Dalton Transactions

PAPER

View Article Online
View Journal | View Issue

Cite this: *Dalton Trans.*, 2019, **48**, 13293

Pathways towards true catalysts: computational modelling and structural transformations of Zn-polyoxotungstates†

Lubin Ni, ‡§ Robin Güttinger, § C. A. Triana, Bernhard Spingler, Kim K. Baldridge *¶ and Greta R. Patzke *

Current catalysis undergoes a paradigm shift from molecular and heterogeneous realms towards new dynamic catalyst concepts. This calls for innovative strategies to understand the essential catalytic motifs and true catalysts emerging from oxidative transformation processes. Polyoxometalate (POM) clusters offer an inexhaustible reservoir for new noble metal-free catalysts and excellent model systems whose structure–activity relationships and mechanisms remain to be explored. Here, we first introduce a new $\{Zn_nNa_{6-n}(B\text{-}\alpha\text{-}SbW_9O_{33})_2\}$ (n = 3–6) catalyst family with remarkable tuning options of the Zn-based core structure and high activity in H_2O_2-assisted catalytic alcohol oxidation as a representative reaction. Next, high level solution-based computational modelling of the intermediates and transition states was carried out for $[Zn_6Cl_6(SbW_9O_{33})_2]^{12-}$ as a representative well-defined case. The results indicate a radical-based oxidation process with the involvement of tungsten and adjacent zinc metal centers. The $\{Zn_nNa_{6-n}(B\text{-}\alpha\text{-}SbW_9O_{33})_2\}$ series indeed efficiently catalyses alcohol oxidation *via* peroxotungstate intermediates, in agreement with strong spectroscopic support and other experimental evidence for the radical mechanism. Finally, the high performance of $[Zn_6Cl_6(SbW_9O_{33})_2]^{12-}$ was traced back to its transformation into a highly active and robust disordered Zn/W-POM catalyst. The atomic short-range structure of this resting pre-catalyst was elucidated by RMC modelling of the experimental W-L_3 and Zn-K edge EXAFS spectra and supported with further analytical methods. We demonstrate that computational identification of the reactive sites combined with the analytical tracking of their dynamic transformations provides essential input to expedite cluster-based molecular catalyst design.

Received 23rd July 2019,
Accepted 26th July 2019

DOI: 10.1039/c9dt03018b

rsc.li/dalton

1 Introduction

The growing demand for economic and efficient catalysts, in order to tackle current resource challenges, has fuelled the development of tuneable molecular catalysts, such as oxo clusters.[1–3] In parallel, the emerging insight into their dynamic transformations under operational conditions gives rise to new and flexible catalytic concepts, which cross the traditional frontiers between molecular and heterogeneous catalysis.[4–6] This paradigm change in catalysis is impressively embodied by polyoxometalates (POMs) as a growing family of multifunctional oxoclusters.[7,8,9–12] Since POMs are crossing the interface between homogeneous and heterogeneous catalysis, especially in oxidative processes, they attract increasing research interest.[13–16] As the design of stable and economic noble metal-free POM catalysts is a forefront focus of green chemistry,[17–20] establishing their predictive structure–activity relationships is vital to explore the virtually inexhaustible structural pool of POMs.[21–24] Furthermore, understanding the mechanisms of key oxidative organic transformations is vital for the design of sustainable and cost-effective catalysts.[6,25–27] However, maximizing the high application potential of molecular and cluster catalysts requires clear strategies for the challenging identification of their true catalyst nature. Generally, understanding the essential active features of true homogeneous catalysts is indispensable for their informed design.

We present a comprehensive analytical and computational strategy to investigate the dynamic evolution of noble metal-

Department of Chemistry, University of Zurich, Winterthurerstrasse 190, CH-8057 Zurich, Switzerland. E-mail: greta.patzke@chem.uzh.ch

† Electronic supplementary information (ESI) available: Synthetic protocols, computational results and crystallographic data, spectroscopic and thermal analyses, X-ray diffraction patterns and electrochemical studies on all compounds, as well as the corresponding CIF files. CCDC 426348–426359. For ESI and crystallographic data in CIF or other electronic format see DOI: 10.1039/c9dt03018b

‡ Present address: School of Chemistry and Chemical Engineering, Yangzhou University, Yangzhou 225002, Jiangsu, P. R. China.

§ Authors contributed equally to the paper.

¶ Present address: Health Science Platform, Tianjin University, 92 Weijin Road, Nankai District, Tianjin 300072, P. R. China.

free POM catalyst models during alcohol oxidation as a representative benchmark for understanding key oxidative transformations.

First, we introduce a new series of more than ten highly active Zn/Sb-POM catalysts with exceptional tunability of their Zn-core nuclearities sandwiched between two {B-α-SbW_9O_{33}} shells.

This newly synthesized POM series serves as a starting point for comprehensive computational modelling of the catalytic process, which is backed by experimental results (Scheme 1). Furthermore, we reveal crucial features of the complex nature of the actual catalyst involved in subsequent catalytic cycles.

Transition metal substituted sandwich-type POMs (TMSPs) are attractive catalyst building blocks, which embed a variety of metal cores between diverse lacunary POM shell types.[28–32,33–35] The manifold applications of noble metal-free TMSPs, such as the sandwich-type $[Co_4(H_2O)_2(\alpha\text{-}PW_9O_{34})_2]$,[10,36,37] triggered an intense debate concerning their true active species in various catalytic assays. This in turn has raised further need for the speciation of homogeneous POM catalysts and related systems in order to explore their dynamic transformations for targeted catalyst design.[23,38–42]

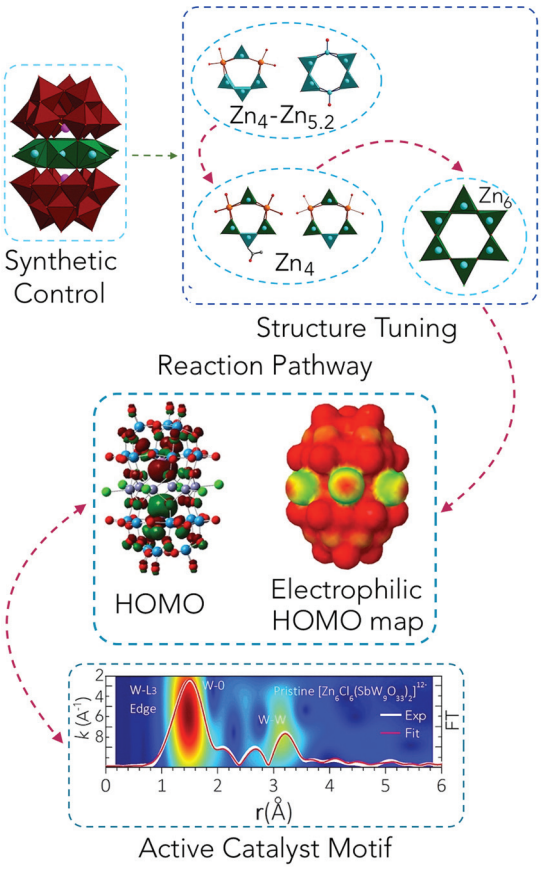

Scheme 1 Structurally tunable and noble metal-free polyoxometalates offer new insight into the modelling and understanding of dynamic catalyst transformations.

The identification of the active centres among the variety of accessible sites of large homogeneous oxocluster catalysts, their speciation in solution, and the detection of their often short-lived competent intermediates, remain demanding tasks.[21,43,44] Furthermore, assigning structural motifs to true catalyst species is a substantial challenge in the absence of long-range structural order.[45–47] Likewise, modelling of transition states and reaction pathways for oxidative organic transformations catalysed by larger molecular clusters, such as POMs, becomes extremely challenging when performed for complete and unrestricted architectures in solvent environments.[48–50] In particular, highly efficient organic transformations with POM catalysts have been identified as excellent model systems forging knowledge into the reactive sites and reaction pathways,[51–53] given that oxidative organic transformation mechanisms are still explored in their own right.[25] Prominent examples include Zn-POM assisted liquid-phase oxidations with hydrogen peroxide,[54–56] as well as recent progress into sandwich-type Zn(II)-containing silicotungstate catalysts.[51,57]

In what follows, our $\{Zn_nNa_{6-n}(B\text{-}\alpha\text{-}SbW_9O_{33})_2\}$ (n = 3–6) POM model systems provide a coherent insight into synthetic control, computational investigations, and catalytic pathways. First, the structure and properties of more than 10 members of this series are discussed. The first step of our analysis is a full-scale solution-based computational modelling of intermediates and transition states involved in cyclohexanol oxidation starting from a structurally defined Zn-POM catalyst. Next, this is complemented with a wide range of investigations into the catalytic activity, the involved intermediates and the analysis of the disordered post-catalytic material. We then implement atomistic Reverse Monte Carlo (RMC) modelling of the EXAFS spectra to elucidate the complex nature of the actual catalytic species giving rise to continuously high catalytic activity over several cycles. This comprehensive strategy sheds new light on essential motifs for designing efficient POM-based oxidation catalysts.

2 Experimental section

2.1 Materials and analytical characterizations

$Na_9[B\text{-}\alpha\text{-}SbW_9O_{33}]\cdot 19.5H_2O$ as a precursor material was prepared according to literature protocols[58] and its purity was confirmed by FT-IR spectroscopy. Other chemicals were commercially purchased and used without further purification. Elemental analyses of all polyanions were performed by Mikroanalytisches Labor Pascher, Remagen, Germany. Fourier transform infrared (FT-IR) spectra were recorded on a Bruker Optics Vertex 70 Spectrometer. Raman spectroscopy was performed on a Renishaw Ramascope 1000 with a green SpectraPhysics Argon laser with a wavelength of 524.5 nm and 50 mW capacity. TG measurements were conducted on a Netzsch STA 449 C between 25 and 800 °C with a heating rate of 5 K min^{-1} in nitrogen atmosphere. UV/vis spectra were recorded on a PerkinElmer Lambda 650S spectrometer. Cyclic

voltammetry experiments were performed on a Metrohm Computrace Voltammetric Analyzer model 757 VA. The system was operated with 757 VA Computrace software (Metrohm). The three-electrode cell system consisted of a 2 mm glassy carbon working electrode (GCE, modified or unmodified), a saturated Ag/AgCl reference electrode and a Pt wire as the counter electrode.

2.2 Catalytic alcohol oxidation

Oxidation reactions were carried out in a 10 mL round-bottom flask. Catalyst, solvent, substrate, and 30% aqueous H_2O_2 were successively placed into the round-bottom flask. A Teflon-coated magnetic stirring bar was added and the reaction mixture was stirred at 85 °C. Detailed reaction conditions are given in the caption of Table 1. All yields reported in this manuscript are based on alcohol conversion. Reaction products were characterized and quantified with a gas chromatograph (Finnigan Trace GC Ultra) equipped with a flame ionization detector and fitted with a ZB-5MS Phenomenex column (30 m length, 0.25 mm internal diameter, 0.25 μm film thickness) using dodecane as the internal reference. Products were furthermore identified by GC-MS (Finnigan Trace DSQ GC-MS systems).

2.3 X-ray absorption spectroscopy

XAS experiments at the W-L_3 and Zn-K edges on solid samples dispersed in cellulose of pristine and post-catalytic $[Zn_6Cl_6(SbW_9O_{33})_2]^{12-}$, and of reference compounds $[WZn_3(H_2O)_2(ZnW_9O_{34})_2]^{12-}$, $[SbW_9O_{33}]^{12-}$ and $Na_2WO_4{\cdot}2H_2O$ were carried out at the SuperXAS beamline at the Swiss Light Source (SLS) at the Paul Scherrer Institut, Villigen, Switzerland. The storage ring was run in top-up mode with an average current of 400 mA. The X-ray beam was collimated using a Si coated mirror and the energy was scanned using a channel-cut Si[111] monochromator. Energy calibration was done using a metal W foil. A toroidal mirror with Rh coating was used after the monochromator to focus the incident X-rays with a spot size of 140 × 120 μm^2 on the samples (photon flux of 3.3 × 10^{11} photons per s). Measurements were done in transmission mode using a 5-element Silicon Drift Detector. The measured EXAFS spectra $k^3\chi(k)$ were extracted by standard data reduction, absorption edge energy calibration and background subtraction as implemented in ATHENA.[59] The spectra were reduced in the range $\Delta k \approx 3$–12 $Å^{-1}$ and Fourier-Transformed to FT$|k^3\chi(k)|$ in the real-space interval $\Delta R \approx 0$–6 Å. To calculate the main values for interatomic distances, coordination numbers (N), and Debye–Waller factors (σ^2), nonlinear least-squares fitting of the FT$|k^3\chi(k)|$ spectra was done with ARTEMIS[59] using the atomic clusters of $[Zn_6Cl_6(SbW_9O_{33})_2]^{12-}$, $[WZn_3(H_2O)_2(ZnW_9O_{34})_2]^{12-}$ (CCDC 1628204), $[SbW_9O_{33}]^{12-}$ (ICSD 406489) and $Na_2WO_4{\cdot}2H_2O$ (ICSD 240882) generated by ATOMS[59] as implemented in IFEFFIT.[59] Amplitudes and phase shifts for single and multiple scattering paths were calculated using the FEFF6 code.[60]

Table 1 Oxidation of cyclohexanol with different Zn-POMs and reference POM catalysts[a]

	Catalyst	Yield[b] (%)
1	**{Zn_4_$Zn_{5.2}$}(1a)**	97
2	**Zn_6(3b)**	>99
3	**Zn_5(5a)**	96
4	**Zn_4(6a)**	95
5	**Zn_3(8)**	98
6	**Zn_6(3b)**[c]	52
7	**Zn_2W_2(9)**	96
8	$[Sb_2W_{22}O_{74}(OH)_2]^{12-}$	92
9	$[SbW_9O_{33}]^{9-}$	77
10	$[Sb^VW_6O_{24}]^{7-}$	60
11	$[H_2W_{12}O_{42}]^{12-}$	73
12	$[P_2W_{18}O_{62}]^{6-}$	21
13	**Zn_6(3b)**[d]	—
14	**Zn_6(3b)**[e]	—
15	**Zn_6(3b)**[f]	—
16	**Zn_6(3b)**[g]	<5

[a] Reaction conditions: 0.25 mmol substrate, 1.25 mmol (30%) H_2O_2, 1.0 μmol catalyst, 1.0 mL H_2O, 85 °C, 7 h. [b] Organic products were identified and quantified by GC-MS and GC with calibrations using pure corresponding standards and dodecane as an internal standard; yield (%) = [cyclohexanone]/initial [cyclohexanol] × 100%. Product distributions were not significantly affected by carrying out the reactions in N_2 atmosphere. [c] 2 mL toluene instead of 1.0 mL H_2O. [d] In the presence of 1.25 mmol hydroquinone. [e] In the presence of 1.25 mmol resorcinol. [f] In the presence of pyrocatechol. [g] In the presence of 1.25 mmol TEMPO.

2.4 Computational details

The conformational analyses of the molecular systems described in this study, including structural and orbital arrangements as well as property calculations, were carried out using the BP86 density functional level of theory[61,62] in combination with (a) the effective core potential/basis set combination, LANL2DZ+f,[63] and (b) Def2-TZVPP basis set.[64] The LANL2DZ basis set is of double-ζ quality in the valence and "valence-1" shells, while the RECP contains Darwin and mass-velocity contributions; f basis functionality was included.[65–67] The Def2-TZVPP basis set is an all electron triple-ζ quality basis set. Full geometry optimizations were performed and uniquely characterized *via* second derivatives (Hessian) analysis to determine the number of imaginary frequencies (0 = minima; 1 = transition state), and the effects of zero point energy. The effects of solvation were taken into account using the COSab method,[68,69] using a dielectric for water and solvent radii from Klamt.[70] Visualization and analysis of structural and property results were obtained using Avogadro[71] and WEBMO.[72]

2.5 Reverse Monte Carlo (RMC)

To simulate the disordered structure of the resting form of the pre-catalyst $[Zn_6Cl_6(SbW_9O_{33})_2]$,[12−] the W-$L_3$ and Zn-K edge EXAFS spectra FT$|k^3\chi(k)|$ [$\Delta r \approx 0$–6 Å] were fitted by RMC simulations as implemented in the RMCProfile.[73] The atoms were constrained to move into cutoff distances W–O ≈ 1.6–2.3 Å, W–W ≈ 3.1–3.8 Å, Zn–O ≈ 1.8–2.8 Å, Zn–Zn ≈ 3.0–3.3 Å and Zn–W ≈ 3.2–3.8 Å. To preserve the bonding, the stretching potentials W–O 0.984 eV (1.99 Å) and Zn–O 0.984 eV (2.2 Å) were used, and their weightings were optimized at each RMC run. RMC-EXAFS fitting was implemented by allowing 1–3% of

atoms to undergo the displacements of ≈0.01–0.03 Å at each RMC run. Total FT$|k^3\chi(k)|$ spectra equal to the averaged single spectrum of each photoabsorbing W and Zn atoms were re-calculated at each RMC run. Each atomic movement was tested according to the consistency R^2 degree between the experimental and refined spectral-data-points as described in detailed references.[74,75]

3 Results and discussion

3.1 Structural characterization & modelling of a new POM catalyst family

3.1.1 Structural characterization of the POM catalyst family. A series of twelve newly synthesized sandwich-type Zn-containing polytungstoantimonates as catalysts for H_2O_2-assisted alcohol oxidation were isolated from the tri-lacunary precursor $Na_9[B\text{-}\alpha\text{-}SbW_9O_{33}]\cdot 19.5\ H_2O$ **{SbW$_9$}** in the presence of $Zn(OAc)_2$ or $Zn(SO_4)_2$ and structurally characterized. Detailed synthetic and analytical information can be found in the ESI.† The initial NH_4^+ concentration was applied as an efficient and straightforward tool to fine-tune the emerging POM structure. The title compounds consist of two identical $[B\text{-}\alpha\text{-}SbW_9O_{33}]^{9-}$ **{SbW$_9$}** units which are linked by a wide variety of Zn^{2+}-containing cores into sandwich-type TMSPs (Fig. 1 and Fig. S1, S12†): $\{[Zn_4Na_2(H_2O)_8(SbW_9O_{33})_2][Zn_{2.6}Na_{0.4}(H_2O)_{2.6}(SbW_9O_{33})]\}^{11-}$ (**1a**, **1b**), $\{[Zn_5NaCl_3(H_2O)_4(SbW_9O_{33})_2][Zn_{5.2}Na_{0.8}(H_2O)_{5.2}(SbW_9O_{33})_2]\}^{17-}$ (**2**), $[Zn_6(H_2O)Cl_5(SbW_9O_{33})_2]^{11-}$ (**3a**) and $[Zn_6Cl_6(SbW_9O_{33})_2]^{12-}$ (**3b**), $[Zn_5Na(H_2O)_5Cl_2(SbW_9O_{33})_2]^{9-}$ (**4**), $[Zn_5Na(H_2O)_5(CH_3COO)_2(SbW_9O_{33})_2]^{9-}$ (**5a**), $[Zn_5Na(H_2O)_4Cl(CH_3COO)_2(SbW_9O_{33})_2]^{10-}$ (**5b**), $[Zn_4Na_2(H_2O)_7(CH_3COO)(SbW_9O_{33})_2]^{9-}$ (**6a**), $[Zn_{4.1}Na_{1.9}Cl_3(H_2O)_7(CH_3COO)(SbW_9O_{33})_2]^{12-}$ (**6b**), $[Zn_4Na_2Cl_3(H_2O)_5(SbW_9O_{33})_2]^{11-}$ (**6c**), $[Zn_{3.5}Na_{2.5}Cl_2(H_2O)_{6.5}(SbW_9O_{33})_2]^{10-}$ (**7**).

Detailed structural data and representations for all members can be found in the ESI (Tables S1–S3 and Fig. S1–S12†). $[Zn_6Cl_6(SbW_9O_{33})_2]^{12-}$ **Zn$_6$(3b)** was selected as a representative structural example, because fully Zn substituted hexagon-sandwich POMs are very rare to date with $[Zn(H_2O)_6(B\text{-}\alpha\text{-}SbW_9O_{33})_2]^{6-}$ being the only recent example reported hitherto from a different synthetic strategy.[76] **Zn$_6$(3b)** consists of two $[B\text{-}\alpha\text{-}SbW_9O_{33}]^{9-}$ units connected by a hexagonal Zn_6 ring $[Zn_6Cl_6O_{12}]$ with D_{3d} symmetry (Fig. 1a). Each of the zinc atoms displays a related five-fold coordinated $[ZnO_4Cl]$ environment with square-pyramidal geometry, consisting of four terminal oxygen atoms from two $\{SbW_9\}$ units with Zn–O bond lengths of 2.061(8)–2.077(8) Å and one chlorine atom Zn–Cl, with a bond length of 2.222(1) Å (Fig. 1b). Six zinc atoms form an approximately equatorial hexagon by sharing their oxygen atoms (Fig. 1b). The remaining members of the $\{Zn_nNa_{6-n}(B\text{-}\alpha\text{-}SbW_9O_{33})_2\}$ (n = 3–6) series either display complete Zn cores, such as in **Zn6(3b)**, or partial substitution of Zn by Na atoms (*cf.* Fig. 1c and ESI† for a detailed description of the individual compounds).

3.1.2 Computational modelling of reaction processes. We first selected **Zn$_6$(3b)** as a representative, highly active and suitably defined structural model for computational simulation of essential steps and motifs in catalytic cyclohexanol oxidation. The further transformation of **Zn$_6$(3b)** under real catalytic con-

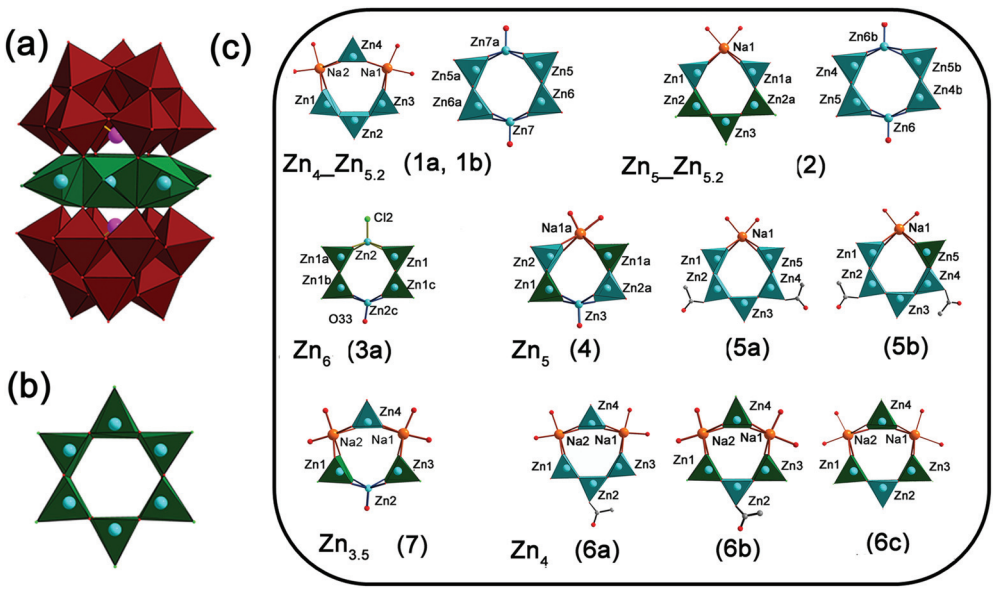

Fig. 1 (a) Polyhedral/ball-and-stick representation of the polyanion $[Zn_6Cl_6(SbW_9O_{33})_2]^{12-}$ **Zn$_6$(3b)**; (b) polyhedral representation of the sandwich-type TM belt $[ZnO_2Cl]_6^{18-}$; (c) polyhedral/ball-and-stick representations of the cluster cores of all the newly characterized Zn-POMs [**Zn$_4$_Zn$_{5.2}$(1a, 1b)**], **Zn$_5$_Zn$_{5.2}$(2)**, **Zn$_6$(3a)**, **Zn$_5$(4)**, colour codes: WO_6 octahedra = red; ZnO_5 square pyramids = blue polyhedra, $Zn(O_4Cl)$ square pyramids = green polyhedra; spheres: W = black, Zn = blue, Sb = pink, O = red, Na = yellow, Cl = green, C = grey; only the most relevant atom is shown on disordered positions for clarity.

ditions will then be discussed in part 2. Therein we discovered that the catalytic process was actually driven by disordered active species emerging from **Zn_6(3b)** as a pre-catalyst. These species were not a suitable target for calculations on the present level as explained in detail below. In the following, we also refer to the isolated, resting form of the pre-catalyst alternatively as the "actual catalyst" for brevity.

A peroxometal-mediated catalytic pathway for cyclohexanol oxidation with hydrogen peroxide in the presence of **Zn_6(3b)** and analogous catalysts is proposed that is based on two fundamental reaction processes. The first step, pathway A.1, involves the reaction of **Zn_6(3b)** with H_2O_2, and the second step, pathway A.2, involves further reaction with cyclohexanol giving back **Zn_6(3b)** in addition to water and cyclohexanone (Fig. 2). To investigate these pathways in the catalytic process in more detail, DFT calculations using the BP86 density functional, suitable for metal containing systems, were carried out. Both double and triple-ζ level basis sets were investigated to ensure self-consistency, including BP86/LANL2DZ+f and BP86/Def2-TZVPP levels of theory (for computational details *cf.* ESI†).

In the first reaction process, A.1, BP86/Def2-TZVPP (BP86/LANL2DZ+f) theory indicates the formation of a tungsten-peroxo (**A.1.a**) species either directly or by first passing through an intermediate tungsten-hydroperoxo (**A.1.inta**) species. In the former case, transition state **A.1.tsa** forms with an activation energy of 22.5 (25.7) kcal mol^{-1} and directly generates **A.1.a**. In the 2-step process, the intermediate structure **A.1.inta** is first generated subsequent to the transition state formation, **A.1.tsa**, which is 19.1 (10.6) kcal mol^{-1} higher in energy than the initial reaction species. Progression to **A.1.a** then proceeds through a second transition state, **A.1.tsb**, with a barrier of 8.2 (10.9) kcal mol^{-1}. In either case, the overall reaction process is exothermic by ~5 kcal mol^{-1} (~thermoneutral for BP86/LANL2DZ+f, −0.5 kcal mol^{-1}).

Further reaction of **A.1.a** with cyclohexanol (pathway **A.2**) results in the formation of a second intermediate, **A.2.inta**, by way of transition state **A.2.tsa**, with a barrier of 28.9 (22.1) kcal mol^{-1}. A vertical O–O group analogue of **A.1.a** was found ~3.4 kcal mol^{-1} higher in energy. This latter structure, **A.1.a-vertical**, has the O–O vertical, with one of the O atoms farther away from the tungsten atom than in **A.1.a** (1.947 Å *vs.* 1.960 Å), indicating an opening up of the W–O–O moiety. Additionally, the O–O bond length is elongated (from 1.475 to 1.483 Å). This facilitates interaction with the cyclohexanol. The transition state, **A.2.tsa**, involves proton transfer from the OH of the cyclohexanol to the peroxo group.

Further computational investigations of subsequent loss of water all strongly indicated the presence of a radical process, as no stable transition state structures could be elucidated. Moreover, computed structures revealed elongation of the O–O bond of the hydroperoxo group, and provided evidence for dissociation of an $^{\bullet}OH$ radical from the hydroperoxo moiety by O–O bond homolysis.[25,77,78] Given the extensive nature of the present calculations, we then proceeded to obtain further experimental evidence for the proposed radical process (section 3.2.1.3. below).

The calculations of the Zn-POMs support the oxidative stability of the polyoxotungstate ligands. The highest occupied molecular orbitals (HOMOs) of the ground state of **Zn_6(3b)** and W-peroxo {**Zn_6**} species (**A.1.a**) have density primarily on tungstate and antimony (Fig. 3d and Fig. S28a–c†). Electrophilic HOMO plots show the highest probability of attack by an electrophile at a favourable position for the H_2O_2-assisted formation of the peroxometalate complex (Fig. 3b).

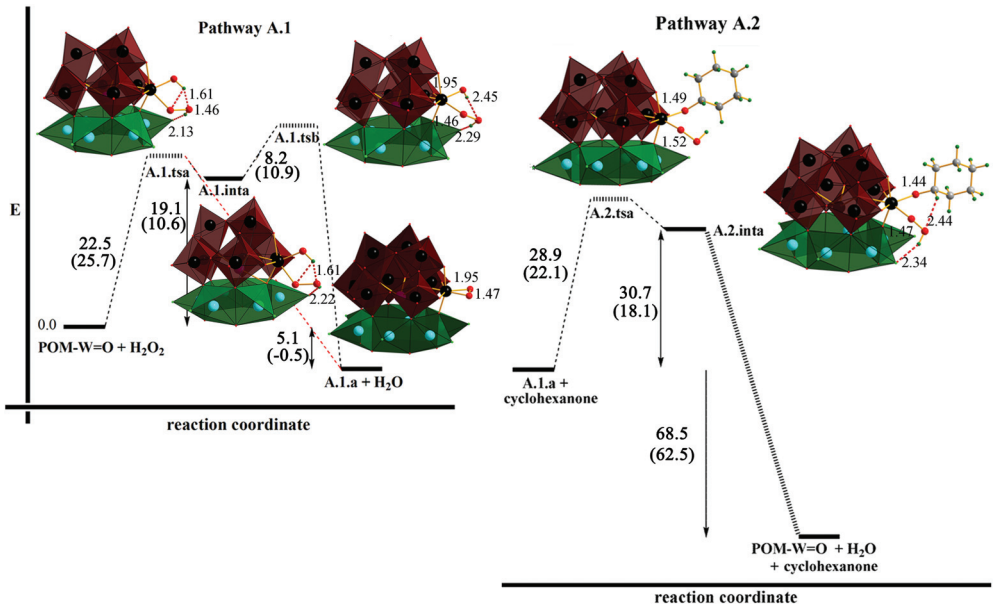

Fig. 2 BP86/Def2-TZVPP (BP86/LANL2DZ+f) potential energy profile (kcal mol^{-1}) for cyclohexanol oxidation with H_2O_2 catalysed by **Zn_6(3b)** in solvent environments (parts of the POM have been omitted for clarity).

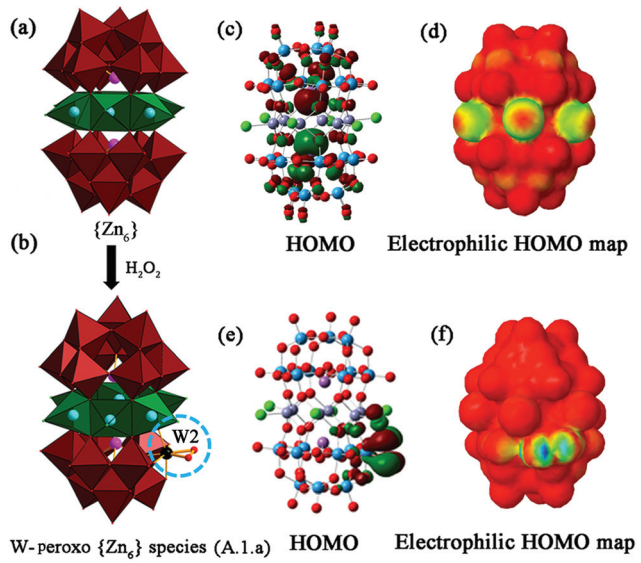

Fig. 3 BP86/Def2-TZVPP optimized structure of (a) **Zn_6(3b)** and (b) W-peroxo {Zn_6} species (A.1.a), depiction of (c) HOMO for **Zn_6(3b)**, (d) electrophilic HOMO map for **Zn_6(3b)**, (e) HOMO for W-peroxo {Zn_6} species, (f) electrophilic HOMO map for W-peroxo {Zn_6} species; blue/red = highest/lowest probability of electrophilic attack.

A comparison of intermediate structures generated by attack at the side oxygen atoms *vs.* the bottom of the peroxometalate structure indicates a higher probability of attack at the side position.

A further look into the molecular orbitals of several of the intermediate structures reveals that the tungsten centres (such as W2 or W3a in Fig. 1a) in fact are active sites in the vicinity of the zinc metal belt, which are most likely responsible for the oxidation reaction (Fig. 3c, d and Fig. S28†). We observe zinc metal centre involvement, indicating an essential cooperative effect on the activation of hydroperoxo or peroxo-tungstate species (Fig. 3e, f and Fig. S29†).

The essential insight from our calculation results, namely a radical process with zinc metal centres involved, also becomes evident from the following investigations of catalytic performance and kinetics.

3.2 Catalytic screening and key features of the true catalyst

3.2.1 Catalytic behaviour of the Zn-POM family

3.2.1.1 Catalytic performance. The series of sandwich-type Zn-containing polytungstoantimonates were investigated for cyclohexanol oxidation as a representative model substrate for alcohol oxidation performance, and all members exhibit remarkably high catalytic activities (Table 1). Cyclohexanol was reacted with hydrogen peroxide and the sandwich-type Zn-POM catalysts (**Zn_4_$Zn_{5.2}$(1a)**, **Zn_6(3b)**, **Zn_5(5a)**, **Zn_4(6a)**, **Zn_3(8)**) in a biphasic reaction system (organic substrate/water), under aerobic conditions at 85 °C for 7 h to afford high yields (around 95–99%) of cyclohexanone throughout (Table 1, entries 1–5). The oxidation proceeds less efficiently at 85 °C in organic media, probably due to the low solubility of the POM catalysts (*cf.* Table 1, entry 6: 52% yield in toluene). Moreover, cyclohexanone yields at 50 °C (7 h) dropped to 26–31% (Table S8,† entries 1–5), *i.e.* elevated reaction temperatures notably improve the conversion rates into cyclohexanone.

Reference experiments with different Zn/Sb- and Sb-polyoxotungstate architectures revealed that the efficiency of alcohol oxidation is not directly related to the absolute number of tungsten centres, *i.e.* the structure of the POM building blocks exerts an important influence (further details can be found in the ESI†).

3.2.1.2 Kinetic investigations of the Zn-POM series. Kinetic studies on cyclohexanol oxidation with the Zn-substituted POMs (**Zn_4_$Zn_{5.2}$(1a)**, **Zn_6(3b)**, **Zn_5(5a)**, **Zn_4(6a)**, and **Zn_3(8)**) are summarized in Fig. 4. Cyclohexanol oxidation proceeded much faster with **Zn_6(3b)** and **Zn_4_$Zn_{5.2}$(1a)** than with other

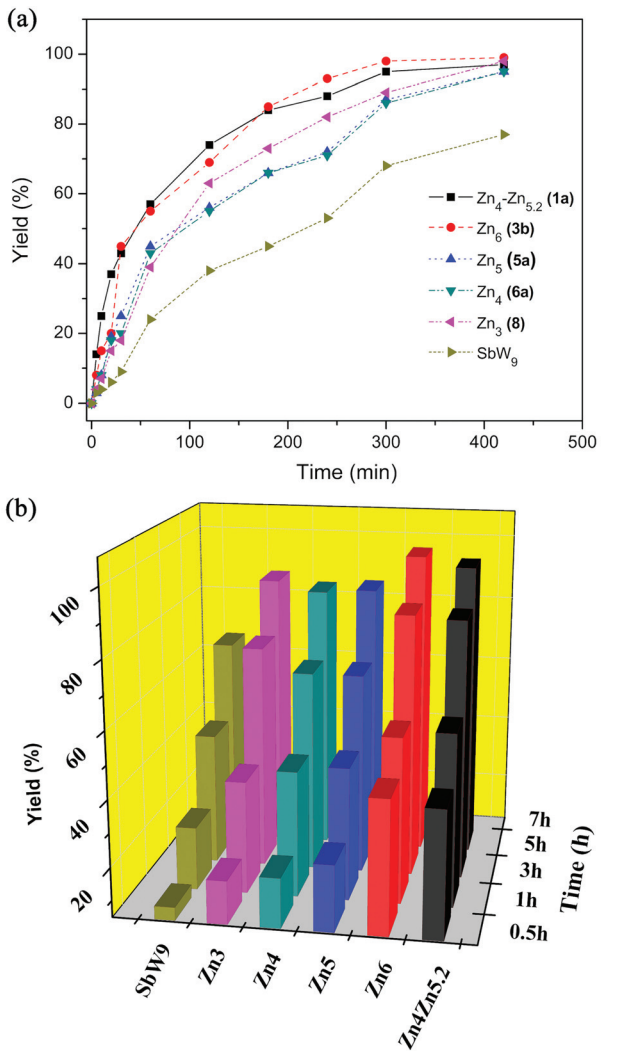

Fig. 4 (a) Kinetic profiles for the oxidation of cyclohexanol catalysed by **{Zn_4_$Zn_{5.2}$}(1a)**, **Zn_6(3b)**, **Zn_5(5a)**, **Zn_4(6a)**, **Zn_3(8)** and **{SbW_9}** ligand (reaction conditions: 1.0 μmol catalyst: 0.25 mmol alcohol, 1.25 mmol H_2O_2 (30%), T = 85 °C, yield (%) = [cyclohexanone]/initial [cyclohexanol] × 100%; (b) core nuclearities of Zn-POMs and Sb-containing reference POMs *vs.* kinetic profiles.

Zn-substituted sandwich-type POMs {**Zn$_5$(5a)**, **Zn$_4$(6a)**, and **Zn$_3$(8)**} at 85 °C (Fig. 4a). After only 30 min, ketone yields above 40% were obtained both in the presence of (**1a**) and (**3b**) in comparison with lower yields around 18–25% with (**5a**), (**6a**), and (**8**). Higher yields (93% for **Zn$_6$(3b)**, 88% for **Zn$_4$_Zn$_{5.2}$(1a)**) can be achieved within 4 h, and both are close to maximum reaction efficiency (*ca.* 98% for **Zn$_6$(3b)** and 95% for **Zn$_4$_Zn$_{5.2}$(1a)**) after 5 h.

In contrast, cyclohexanone formation with **Zn$_5$(5a)**, **Zn$_4$(6a)** and **Zn$_3$(8)** afforded lower yields after 4 h (71%, 72%, and 82%, respectively), and maximum yields of 95–98% were achieved only after 7 h. Moreover, the catalytic efficiency of **{SbW$_9$}** is lower than for all of the Zn-containing POMs ((**1a**), (**3b**), (**5a**), (**6a**), and (**8**)). Kinetic studies indicate that the initial zinc core nuclearity affects the catalytic properties of sandwich-type Zn-substituted POMs (**1a–8**) (Fig. 4b).

3.2.1.3 Catalytic reaction pathways. The interaction of the catalysts with H_2O_2 was investigated for $[Zn_6Cl_6(SbW_9O_{33})_2]^{12-}$ **Zn$_6$(3b)** as a representative example. Reference FT-IR and Raman spectra of **Zn$_6$(3b)** in aqueous solution agree well with solid state spectra (Fig. S31 and S32†). FT-IR spectra show a typical peroxo species vibration at 835 cm^{-1} after H_2O_2 addition (Fig. S33b†), as reported previously for the $[SbW_9O_{33}]^{9-}$ and $[WZnRh^{III}(ZnW_9O_{34})_2]^{10-}$ catalysts.[56,79]

After the decomposition of excess H_2O_2 through treatment with aqueous KI solution, the peak at 835 cm^{-1} disappeared and the resulting FT-IR spectrum resembled the pristine $[Zn_6Cl_6(SbW_9O_{33})_2]^{12-}$ polyanion (Fig. S33c†). Likewise, the addition of small amounts of hydrogen peroxide ($[H_2O_2]/[(\mathbf{3b})]$ = 1–5) to a **Zn$_6$(3b)** leads to differences in the Raman spectra in solution compared to pristine **Zn$_6$(3b)** (Fig. S34b–d†). A new weak band appears at 875 cm^{-1}, which arises from the stretching ν(O–O) vibration of H_2O_2.[80,81] Larger amounts of hydrogen peroxide ($[H_2O_2]/[(\mathbf{3b})]$ = 50) turn the solution into a white emulsion within a few minutes at 85 °C.

The obtained Raman spectrum differs considerably from the above results (Fig. S34e†). The intensity of the strongest band at 960 cm^{-1} is decreased and a new rather weak line at 992 cm^{-1} is ascribed to ν_{as}(W=O$_d$) of a new species. Two significant new bands appear at 619 and 556 cm^{-1}, which can be assigned to characteristic stretching vibrations $\nu_s[W(O)_2]$ and $\nu_{as}[W(O)_2]$ of the peroxo unit $[W(O)_2]$.[79] The FT-IR and Raman spectra in their entirety clearly indicate the formation of a W-peroxo species as a plausible intermediate in alcohol oxidation.

Cyclohexanol oxidation was also performed in the presence of an excess of different radical scavengers, namely hydroquinone, resorcinol or pyrocatechol, or with TEMPO (2,2,6,6,-Tetramethyl-piperidin-1-yl)oxyl. The formation of cyclohexanone was not observed in the presence of the first radical scavenger type (R = o-C_6H_4; entries 13–15, Table 1), and a significantly lower cyclohexanone yield was obtained with TEMPO as well (entry 16, Table 1). These results strongly suggest the involvement of a radical mechanism during activation of H_2O_2 by the **{Zn$_6$}** POM catalysts *via* W-peroxo species or W-hydroperoxo species, in line with our computational results.[82,83]

3.2.2 Recycling of Zn6(3b) and key motifs of the true catalyst

3.2.2.1 Recycling behaviour. **Zn$_6$(3b)** was subjected to recycling runs through biphasic separation (for experimental details *cf.* ESI†). Generally, cyclohexanol oxidation catalysed by the recycled **Zn$_6$(3b)** still afforded high yields at 94% after several cycles (Tables S9† and 2). Investigations into the structural features of the actual catalyst were performed for **Zn$_6$(3b)** as a pre-catalyst among the series because it displayed higher activity than other members upon subsequent catalytic cycles.

However, the formation of a precipitate was observed approx. 2 min into the first cycle. This is clearly below inductions of up to 60 min observed in other studies and does not point to the formation of a heterogeneous active catalyst.[52,53] EDX analyses of the isolated solid showed substantial amounts of Sb and very low tungsten contents (Table S13†) together with amorphous structural features (Fig. S35†). No further precipitation was observed during the following recycling runs, and the activity of the true catalyst remaining in the aqueous phase was constantly high after 3 runs (Table S9†). In contrast, the Sb-rich precipitate displayed very low alcohol oxidation activity with yields around 14%.

Subsequently, the reaction was performed with a lower amount of **Zn$_6$(3b)** (0.5 μmol) to investigate the concentration-dependence of the Sb-rich precipitate formation. Precipitation decreased significantly and was almost not observable anymore. However, the cyclohexanone yield dropped to 65%.

A comparison of the FT-IR and Raman spectra of **Zn$_6$(3b)** with the active catalyst remaining in the aqueous phase (after lyophilisation) and the solid precipitate indicates the presence of a POM-related structure that differs notably from the catalytically inactive solid phase (Fig. 5a). Likewise, the solid precipitate displays different Raman bands from the characteristic POM bands of the active catalyst around 950 cm^{-1} (Fig. 5a).

3.2.2.2 Analytical characterization of the resting pre-catalyst. In order to examine **Zn$_6$(3b)** as a pre-catalyst and its transformation process into the active catalyst, the reaction was scaled up by a factor of 10 (Table 2). Again, the Sb-rich precipitate was removed (*cf.* EDX mapping in Fig. S38†) after the first cycle. The yields afforded by the aqueous phase containing the resting catalytically active species (*cf.* EDX mapping in

Table 2 Recycling experiments with **Zn$_6$(3b)**

Cycle	Cyclohexanone yield (%) **Zn$_6$(3b)**[a]
1	>99
2	98
3	96
4	90
5	75

[a] Reaction conditions: 2.5 mmol substrate, 12.5 mmol (30%) H_2O_2, 10 μmol catalyst **Zn$_6$(3b)**, 10 mL H_2O, 85 °C, 7 h. Yields (%) were determined by GC analyses by using pure corresponding samples as calibration standards and dodecane as an internal standard (reaction was scaled up by a 10-fold dimension of the standard procedure (Table S9†) to enable 5 recycling runs).

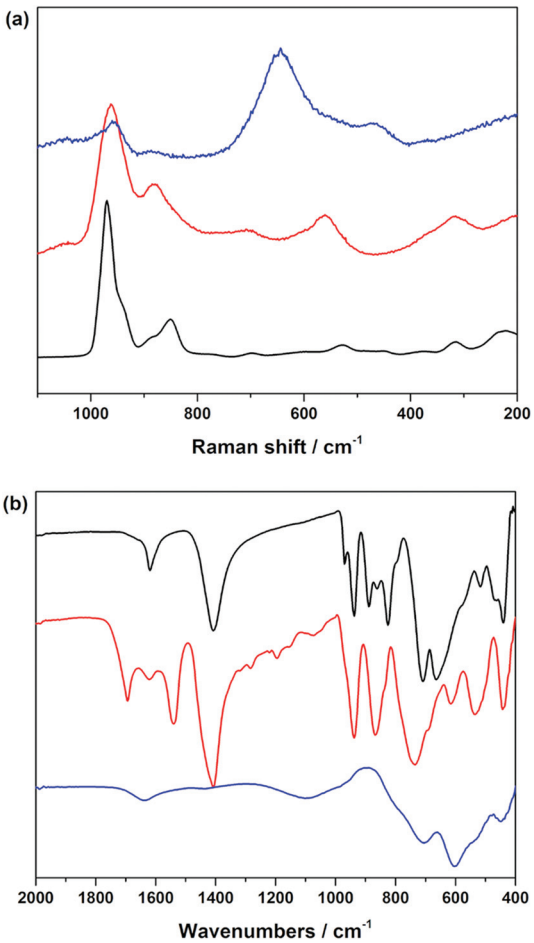

Fig. 5 (a) Raman spectra and (b) FT-IR spectra of as-synthesized **Zn_6(3b)** (black), **Zn_6(3b)** after cyclohexanol oxidation (red) and of the insoluble powder after cyclohexanol oxidation (blue) (solid phase measurements).

Fig. S37†) remained as high as 96% during the third recycling run (Table 2), and no more precipitation was observed during the second cycle. The up-scaled production of the resting pre-catalyst afforded similar FT-IR spectra after the first cycle as shown in Fig. 5b upon removal of the aqueous phase by lyophilisation.

Detailed investigations were performed to understand the atomic-range structure of the highly active POM catalyst emerging from **Zn_6(3b)**. While PXRD patterns recorded after evaporation of the aqueous phase suggest the formation of an amorphous phase (Fig. S36†), the corresponding FT-IR and Raman spectra still strongly point to the presence of a POM-type structure (Fig. 5 and 6). Further attempts to identify its structural features with ^{183}W NMR spectroscopy remained unsuccessful. Therefore, a crystal structure database search for possible analogues to the resting pre-catalyst was carried out, first filtering for Zn/W ratios of 1 : 3.4 (Tables S11 and S12†). The closest but not perfect match was the well-known $[WZn_3(H_2O)_2(ZnW_9O_{34})_2]^{12-}$ (**Zn_3**) POM catalyst.[84] $[ZnW_{12}O_{40}]^{6-}$ was also considered as a representative reference and synthesised from literature procedures.[85]

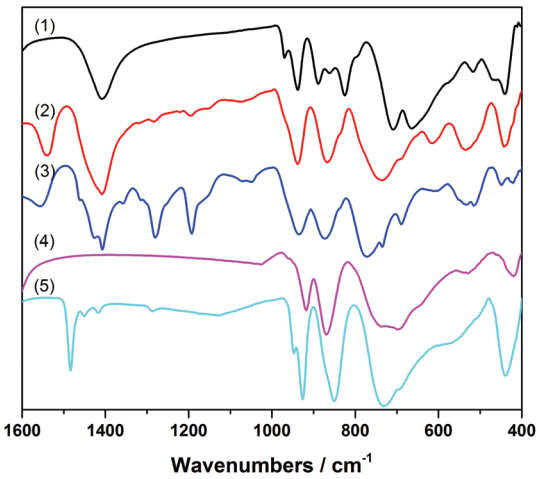

Fig. 6 FT-IR spectra of (1) **Zn_6(3b)** in the solid state, (2) **Zn_6(3b)** after 1st cyclohexanol oxidation (3) **Zn_6(3b)** after 5th cyclohexanol oxidation, (4) $[WZn_3(H_2O)_2(ZnW_9O_{34})_2]^{12-}$ reference in the solid state, (5) $[ZnW_{12}O_{40}]^{6-}$ reference in the solid state.

A comparison of the FT-IR spectra of the highly active POM catalyst emerging from **Zn_6(3b)** after the first and fifth cycle with those of $[WZn_3(H_2O)_2(ZnW_9O_{34})_2]^{12-}$ and of $[ZnW_{12}O_{40}]^{6-}$ (Fig. 6) shows that the FT-IR spectra exhibit a band at 438 cm^{-1}, in agreement with the ν_{as}(Zn–O) mode seen in the reference $\{ZnW_9O_{34}\}$ and $\{ZnW_{12}O_{40}\}$ Keggin-anions. Additional well resolved bands appear around 937 (ν_{as}(W–O_d)), 866 (ν_{as}(W–O_b)) and 737 cm^{-1} (ν_{as}(W–O_c)).[55,86] ICP-MS analyses of the post-catalytic product regenerated from the aqueous phase indicate major leaching of the Sb atoms from **Zn_6(3b)** upon oxidation (0.24% remaining) and a characteristic Zn : W ratio for Zn-polyoxotungstates (Tables S11 and S12†). Since it is well-known that the $\{ZnW_9O_{34}\}$ Keggin-anion is stable under catalytic alcohol oxidation conditions,[55] we suggest that the Keggin half-shells of the highly active POM catalyst emerging from **Zn_6(3b)** adopt a $\{ZnW_9O_{34}\}$ architecture. The sites of the leached Sb atoms are most likely occupied by two Zn atoms, originating from the $[Zn_6O_{12}Cl_6]$ belt. This premise is supported by the obvious similarity observed between the FT-IR spectra of the active POM catalyst and those of the $[WZn_3(H_2O)_2(ZnW_9O_{34})_2]^{12-}$ and $[ZnW_{12}O_{40}]^{6-}$ anions (Fig. 6).

Further investigations on **Zn_5(5b)** and **Zn_4(6a)** as representative members of the Zn-POM family also showed antimony loss as a precipitate formed after the first catalytic cycle (*cf.* EDX analyses in Table S14†). PXRD patterns of the isolated post-catalytic forms of **Zn_5(5b)** and **Zn_4(6a)** furthermore show that both of them are amorphous (Fig. S39†). Both POMs also clearly display significant changes in their post-catalytic FT-IR patterns (Fig. S40†).

3.2.2.3 Key structural features of the true catalyst. To further support the presence of *de novo* created $\{ZnW_9O_{34}\}$ Keggin moieties in the structure of the true catalyst arising from **Zn_6(3b)** upon cyclohexanol oxidation, the W-L_3 and Zn-K edge EXAFS spectra were measured. Those of pristine **Zn_6(3b)** and

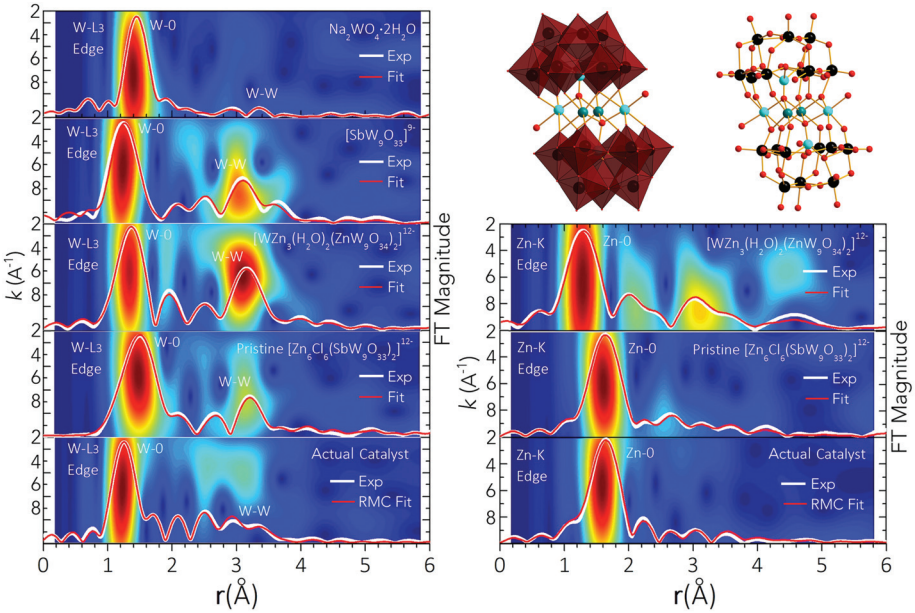

Fig. 7 Nonlinear least-squares fitting (red) of the experimental W-L_3 and Zn-K edge EXAFS spectra FT|$k^3\chi(k)$| (white) of pristine $[Zn_6Cl_6(SbW_9O_{33})_2]^{12-}$ and those of the reference compounds $Na_2WO_4{\cdot}2H_2O$, $Na_9[SbW_9O_{33}]$, $Na_{12}[WZn_3(H_2O)_2(ZnW_9O_{34})_2]$. The experimental W-$L_3$ and Zn-K edge FT|$k^3\chi(k)$| spectra of the resting pre-catalyst (white, bottom) were simulated by RMC-EXAFS fitting (red, bottom). The background 2D contour plot is the Wavelet–Transformed (WT) of the $k^3\chi(k)$ spectra. Representative RMC-EXAFS optimized structures of the resting pre-catalyst are shown at the top right side as polyhedral and ball and stick representation (black, tungsten; red, oxygen; light blue, zinc; teal, Zn/W).

those of $[WZn_3(H_2O)_2(ZnW_9O_{34})_2]^{12-}$, $Na_2WO_4{\cdot}2H_2O$ and $[SbW_9O_{33}]^{9-}$ were recorded as references (Fig. 7). The main calculated values for interatomic distances, atomic coordination numbers and Debye–Waller factors (σ^2), are summarized in Tables S15 and 16.† When comparing the Fourier-FT $|k^3\chi(k)|$ and Wavelet-Transformed (WT) spectra of the resting pre-catalyst with those of $Na_2WO_4{\cdot}2H_2O$, it is noted that the peaks in FT|$k^3\chi(k)$| at $r \approx 1.6$–3.6 Å, and the maxima in the WT ($r \approx 2.5$–3.1 Å at $k \approx 3.0$–7.0 Å^{-1}) of the resting pre-catalyst are not present in the $Na_2WO_4{\cdot}2H_2O$ spectra. This indicates that the structure motif present in the actual catalyst is different from the tetrahedral tungsten environment of $Na_2WO_4{\cdot}2H_2O$. Instead, the first W–O and Zn–O coordination shells in the FT|$k^3\chi(k)$| and WT spectra of the catalyst isolated after cyclohexanol oxidation show similar features as those of the pristine **Zn_6(3b)**, $[WZn_3(H_2O)_2(ZnW_9O_{34})_2]^{12-}$, and $[SbW_9O_{33}]^{9-}$ POMs. This suggests that the structural Keggin motif is preserved in the final catalyst to a large extent, which agrees with the analysis of the FT-IR and Raman spectra (Fig. 5, 6, S26 and S27†). The W-W shell in the FT|$k^3\chi(k)$| and WT spectra of the isolated catalytic species shows low intensity and broadened features due to the distorted character of the $\{ZnW_9O_{34}\}$ moieties. The low-Z and high-Z elements scatter more effectively at low and high k-values, respectively. The WT spectra of **Zn_6(3b)** and $[SbW_9O_{33}]^{9-}$ display maxima at $k \approx 8.92$ Å^{-1} at $r \approx 3.18$ Å and $r \approx 3.02$ Å, respectively, due to scattering from Sb atoms. The maximum in the WT spectra of $[WZn_3(H_2O)_2(ZnW_9O_{34})_2]^{12-}$ shifts to a low k-value of ≈6.1 Å^{-1} at $r \approx 3.17$ Å due to the lower Z value of scattering Zn atoms. No Sb-K edge EXAFS signal in the resting pre-catalyst was obtained due to the major leaching of Sb atoms, and neither did the W-L_3 or Zn-K edge WT spectra of the resting pre-catalyst show maxima attributed to scattering from Sb atoms.

Therefore, the shift in the maximum of the WT spectra of the emerging catalyst to $k \approx 4.8$ Å^{-1} at $r \approx 2.48$–3.09 Å, is associated with the low Z value of O and Zn atoms from the *de novo* created $\{ZnW_9O_{34}\}$ Keggin anion. The lower intensity and broadening of the maxima in the WT spectra of the actual catalyst is due to the distorted character of these $\{ZnW_9O_{34}\}$ moieties.

To further understand the atomic-scale structure and stability of the true catalyst, RMC-EXAFS fitting of the experimental W-L_3 and Zn-K edge FT|$k^3\chi(k)$| spectra (Fig. 7 and Tables S15, 16†) was implemented (see Methods). Representative RMC-EXAFS optimized structures are shown in Fig. 7. The results indicate that, in the isolated form of the catalyst, the W atoms are still six-fold coordinated with neighbouring O atoms, one of which is bound to the Zn atoms of the *de novo* created $\{ZnW_9O_{34}\}$ Keggin anion. While the overall POM structure is generally conserved upon cyclohexanol oxidation, the W–O octahedra display a distorted structure. The distribution of W–O interatomic distances is spread over the range W–O ≈ 1.63–2.25 Å (Table S15†). The W–W shell also attains a distorted architecture. In the pristine **Zn_6(3b)** there are two W atoms at the same distance from a central W atom. However, this order does not exist in the resting pre-catalyst, where W atoms are coordinated at distances W–W ≈ 3.194, 3.472, 3.651, 3.840 Å. The Zn atoms linking the $\{ZnW_9O_{34}\}$ Keggin moieties

are six-fold coordinated in distorted $\{ZnO_6\}$ octahedral units (Fig. 7 and Tables S15, 16†), with two half occupied Zn sites (Zn/W ratio of 1 : 3.8). The distorted character of these $\{ZnO_6\}$ octahedra leads to out-of-centre alignment of the $\{ZnW_9O_{34}\}$ Keggin-moieties. EDX analysis showed small amounts of W in the insoluble precipitate (1.4%, Table S13†), and thus, the formation of a small number of defective $\{ZnW_9O_{34-x}\}$ moieties cannot be ruled out. Single spatial rotation of the Keggin-moieties is also likely to occur, which is in line with the amorphous profile observed in the PXRD pattern recorded after evaporation of the aqueous phase (Fig. S36†). As short-range order RMC-EXAFS fitting converges to the "average" of structures, the *de novo* created highly active POM catalyst emerging from **Zn_6(3b)** must thus be treated as an ensemble of closely related, but non-identical POM-like units. As such, this complex and structurally less defined composition of the actual catalyst would not be a suitable target for computational modelling on the high level used in the present study.

Interestingly, previous computational studies on structurally related $\{[WZnTM_2(H_2O)_2](ZnW_9O_{34})_2\}^{n-}$ (TM = Rh^{III}, Pd^{II}, and Pt^{II}) POMs revealed that the analogous positions in the belt where the mixed W/Zn centres are located in $[WZn_3(H_2O)_2(ZnW_9O_{34})_2]^{12-}$ are sterically hindered during H_2O_2 activation, so that they are rather unlikely to participate in alcohol oxidation in the present case.[87] From a dynamic perspective, the complex spatial distribution of inequivalent POM units and the defective half-occupancy of Zn atoms provide energetic and structural flexibility to the *de novo* created POM architecture while preserving the bonding around the active W/Zn catalytic centres responsible for the activation of hydroperoxo and peroxo-tungstate species. This could also explain the catalytic stability observed in the $\{ZnW_9O_{34}\}$ Keggin anion under catalytic cyclohexanol oxidation.[55]

4 Conclusions

Starting from polyoxometalates as model systems for the investigation of true catalyst transformations, more than ten $\{Zn_nNa_{6-n}(B\text{-}\alpha\text{-}SbW_9O_{33})_2\}$ (n = 3–6) sandwich-type catalysts were synthesized from a straightforward and tuneable protocol. We present a systematic three-step strategy for unravelling the key phenomena behind their high catalytic activity in homogeneous alcohol oxidation as a convenient benchmark process.

(1) The observed high catalytic performance was experimentally assigned to tungsten peroxo-species as plausible intermediates. Zero or drastically reduced yields in the presence of scavengers strongly suggest the presence of a radical-assisted process.

(2) These experimental results were supported with high level solution-based computational modelling of the oxidation process with $[Zn_6Cl_6(SbW_9O_{33})_2]^{12-}$ in solvent environments. A plausible mechanism *via* tungsten centres in the vicinity of the Zn-based core structure is presented, which exerts a co-operative effect on peroxide activation. Both the formation of a W–O–O-based catalytic intermediate and its regeneration *via* a rapid radical-based alcohol oxidation process without subsequent stable transition states correspond with the obtained spectroscopic data and catalytic characterizations.

(3) Detailed post-catalytic investigations of structural transformations furthermore establish that the true catalyst arising from the best performing $[Zn_6Cl_6(SbW_9O_{33})_2]^{12-}$, which remains active over 5 cycles is in fact a Sb-deprived Zn-POM. As elucidating the disordered features of this true catalyst after isolation from solution posed a substantial challenge, we implemented RMC-EXAFS fitting of the experimental W-L_3 and Zn-K edge EXAFS spectra using $[WZn_3(H_2O)_2(ZnW_9O_{34})_2]^{12-}$ as a plausible reference model for the obtained analytical fingerprint of the resting form of the actual catalyst. The presence of a Zn-belt sandwiched between B-α-$[ZnW_9O_{34}]^{12-}$ shells in the true catalyst complies well with the established modelling premises and the obtained analytical data.

Our results demonstrate that detailed computational modelling in combination with a rigorous examination of catalytic pathways reveals the underlying essential reaction steps and crucial structural motifs of polyoxometalate catalysts. Such multiperspective strategies can notably expedite the design of robust catalysts from the wide structural parameter space of oxoclusters.

Conflicts of interest

There are no conflicts to declare.

Acknowledgements

The authors thank the Swiss National Science Foundation (SNSF Professorship PP00P2_133483/1 and Sinergia Grant No. CRSII2_136205/1), the University of Zurich and the UZH Research Priority Program (URPP) for Solar Light to Chemical Energy Conversion (LightChEC) for financial support. K. K. B. acknowledges the Qian Ren Scholar Program of China. L. N. thanks the University of Zurich for support of his PhD thesis work with a Forschungskredit grant, and the National Natural Science Foundation of China (Grant No. 21401162) as well as the Priority Academic Program Development of Jiangsu Higher Education Institutions.

References

1 L. MacDonald, B. Rausch, M. D. Symes and L. Cronin, *Chem. Commun.*, 2018, **54**(9), 1093.
2 A. M. Khenkin, M. Somekh, R. Carmieli and R. Neumann, *Angew. Chem., Int. Ed.*, 2018, **57**(19), 5403.
3 R. J. Errington, B. Kandasamy, D. Lebbie and T. Izuagie, in *Polyoxometalate-based assemblies and functional materials*, ed. Y.-F. Song, Springer, Cham, 2018, p. 139.
4 J. J. Stracke and R. G. Finke, *ACS Catal.*, 2014, **4**(3), 909.
5 D. B. Eremin and V. P. Ananikov, *Coord. Chem. Rev.*, 2017, **346**, 2.

6 B. Chakraborty, G. Gan-Or, M. Raula, E. Gadot and I. A. Weinstock, *Nat. Commun.*, 2018, **9**(1), 4896.
7 J. Li, R. Güttinger, R. Moré, F. Song, W. Wan and G. R. Patzke, *Chem. Soc. Rev.*, 2017, **46**, 6124.
8 Q. Yin and C. L. Hill, *Nat. Chem.*, 2018, **10**(1), 6.
9 P. Kögerler, B. Tsukerblat and A. Müller, *Dalton Trans.*, 2010, **39**(1), 21.
10 W. Liu, W. Mu, M. Liu, X. Zhang, H. Cai and Y. Deng, *Nat. Commun.*, 2014, **5**, 3208.
11 H. G. T. Ly, G. Fu, A. Kondinski, B. Bueken, D. de Vos and T. N. Parac-Vogt, *J. Am. Chem. Soc.*, 2018, **140**(20), 6325.
12 C. Falaise, M. A. Moussawi, S. Floquet, P. A. Abramov, M. N. Sokolov, M. Haouas and E. Cadot, *J. Am. Chem. Soc.*, 2018, **140**(36), 11198.
13 S. J. Folkman, J. Soriano-Lopez, J. R. Galán-Mascarós and R. G. Finke, *J. Am. Chem. Soc.*, 2018, **140**(38), 12040.
14 K. P. Sullivan, M. Wieliczko, M. Kim, Q. Yin, D. L. Collins-Wildman, A. K. Mehta, J. Bacsa, X. Lu, Y. V. Geletii and C. L. Hill, *ACS Catal.*, 2018, **8**(12), 11952.
15 H. Yu, S. Ru, G. Dai, Y. Zhai, H. Lin, S. Han and Y. Wei, *Angew. Chem., Int. Ed.*, 2017, **56**(14), 3867.
16 G. Zhao, F. Yang, Z. Chen, Q. Liu, Y. Ji, Y. Zhang, Z. Niu, J. Mao, X. Bao, P. Hu and Y. Li, *Nat. Commun.*, 2017, **8**, 14039.
17 P.-E. Car, M. Guttentag, K. K. Baldridge, R. Alberto and G. R. Patzke, *Green Chem.*, 2012, **14**(6), 1680.
18 S. Tanaka, M. Annaka and K. Sakai, *Chem. Commun.*, 2012, **48**(11), 1653.
19 S. Goberna-Ferrón, J. Soriano-López, J. R. Galán-Mascarós and M. Nyman, *Eur. J. Inorg. Chem.*, 2015, **2015**(17), 2833.
20 M. Natali, I. Bazzan, S. Goberna-Ferrón, R. Al-Oweini, M. Ibrahim, B. S. Bassil, H. Dau, F. Scandola, J. R. Galán-Mascarós, U. Kortz, A. Sartorel, I. Zaharieva and M. Bonchio, *Green Chem.*, 2017, **19**(10), 2416.
21 K. Kamata, K. Yonehara, Y. Nakagawa, K. Uehara and N. Mizuno, *Nat. Chem.*, 2010, **2**(6), 478.
22 S. Schönweiz, M. Heiland, M. Anjass, T. Jacob, S. Rau and C. Streb, *Chem. – Eur. J.*, 2017, **23**(61), 15370.
23 Q. Han, B. Qi, W. Ren, C. He, J. Niu and C. Duan, *Nat. Commun.*, 2015, **6**, 10007.
24 S.-S.-Y. Wang, *Chem. Rev.*, 2015, **115**(11), 4893.
25 M. Sankar, E. Nowicka, E. Carter, D. M. Murphy, D. W. Knight, D. Bethell and G. J. Hutchings, *Nat. Commun.*, 2014, **5**, 3332.
26 F. Lucarini, M. Pastore, S. Vasylevskyi, M. Varisco, E. Solari, A. Crochet, K. M. Fromm, F. Zobi and A. Ruggi, *Chem. – Eur. J.*, 2017, **23**(28), 6768.
27 P. Melle, Y. Manoharan and M. Albrecht, *Inorg. Chem.*, 2018, **57**(18), 11761.
28 Y. Yang, B. Zhang, Y. Wang, L. Yue, W. Li and L. Wu, *J. Am. Chem. Soc.*, 2013, **135**(39), 14500.
29 X.-B. Han, Y.-G. Li, Z.-M. Zhang, H.-Q. Tan, Y. Lu and E.-B. Wang, *J. Am. Chem. Soc.*, 2015, **137**(16), 5486.
30 M. Martin-Sabi, J. Soriano-López, R. S. Winter, J.-J. Chen, L. Vilà-Nadal, D.-L. Long, J. R. Galán-Mascarós and L. Cronin, *Nat. Catal.*, 2018, **1**(3), 208.
31 G. Gao, F. Li, L. Xu, X. Liu and Y. Yang, *J. Am. Chem. Soc.*, 2008, **130**(33), 10838.
32 Y. Liu, S. Liu, D. He, N. Li, Y. Ji, Z. Zheng, F. Luo, S. Liu, Z. Shi and C. Hu, *J. Am. Chem. Soc.*, 2015, **137**(39), 12697.
33 T. McGlone, L. Vila-Nadal, H. N. Miras, D.-L. Long, J. M. Poblet and L. Cronin, *Dalton Trans.*, 2010, **39**(48), 11599.
34 M.-A. Pilette, S. Floquet, J. Marrot, F. Sécheresse and E. Cadot, *Eur. J. Inorg. Chem.*, 2013, **2013**(10–11), 1726.
35 L.-H. Bi, M. Reicke, U. Kortz, B. Keita, L. Nadjo and R. J. Clark, *Inorg. Chem.*, 2004, **43**(13), 3915.
36 Q. Yin, J. M. Tan, C. Besson, Y. V. Geletii, D. G. Musaev, A. E. Kuznetsov, Z. Luo, K. I. Hardcastle and C. L. Hill, *Science*, 2010, **328**(5976), 342.
37 Z. Huang, Z. Luo, Y. V. Geletii, J. W. Vickers, Q. Yin, D. Wu, Y. Hou, Y. Ding, J. Song, D. G. Musaev, C. L. Hill and T. Lian, *J. Am. Chem. Soc.*, 2011, **133**(7), 2068.
38 J. W. Vickers, H. Lv, J. M. Sumliner, G. Zhu, Z. Luo, D. G. Musaev, Y. V. Geletii and C. L. Hill, *J. Am. Chem. Soc.*, 2013, **135**(38), 14110.
39 F. Evangelisti, R. Güttinger, R. Moré, S. Luber and G. R. Patzke, *J. Am. Chem. Soc.*, 2013, **135**(50), 18734.
40 M. Zheng, Y. Ding, X. Cao, T. Tian and J. Lin, *Appl. Catal., B*, 2018, **237**, 1091.
41 S. Reinoso, B. Artetxe and J. M. Gutiérrez-Zorrilla, *Acta Crystallogr., Sect. C: Struct. Chem.*, 2018, **74**(Pt 11), 1222.
42 J. M. Cameron, J. Gao, D.-L. Long and L. Cronin, *Inorg. Chem. Front.*, 2014, **1**(2), 178.
43 R. Neumann and M. Dahan, *Nature*, 1997, **388**(6640), 353.
44 R. E. Schreiber, H. Cohen, G. Leitus, S. G. Wolf, A. Zhou, L. Que and R. Neumann, *J. Am. Chem. Soc.*, 2015, **137**(27), 8738.
45 E. Willinger, C. Massué, R. Schlögl and M. G. Willinger, *J. Am. Chem. Soc.*, 2017, **139**(34), 12093.
46 M. A. Caro, A. Aarva, V. L. Deringer, G. Csányi and T. Laurila, *Chem. Mater.*, 2018, **30**(21), 7446.
47 J. S. Kim, I. Park, E.-S. Jeong, K. Jin, W. M. Seong, G. Yoon, H. Kim, B. Kim, K. T. Nam and K. Kang, *Adv. Mater.*, 2017, **29**(21), 1606893.
48 N. S. Antonova, J. J. Carbo, U. Kortz, O. A. Kholdeeva and J. M. Poblet, *J. Am. Chem. Soc.*, 2010, **132**(21), 7488.
49 P. Jimenez-Lozano, I. D. Ivanchikova, O. A. Kholdeeva, J. M. Poblet and J. J. Carbo, *Chem. Commun.*, 2012, **48**(74), 9266.
50 B. B. Sarma, I. Efremenko and R. Neumann, *J. Am. Chem. Soc.*, 2015, **137**(18), 5916.
51 Y. Kikukawa, K. Yamaguchi and N. Mizuno, *Angew. Chem., Int. Ed.*, 2010, **49**(35), 6096.
52 L. Ni, J. Patscheider, K. K. Baldridge and G. R. Patzke, *Chem. – Eur. J.*, 2012, **18**(42), 13293.
53 S. R. Amanchi, A. M. Khenkin, Y. Diskin-Posner and R. Neumann, *ACS Catal.*, 2015, **5**(6), 3336.
54 C. M. Tourné, G. F. Tourné and F. Zonnevijlle, *J. Chem. Soc., Dalton Trans.*, 1991, **107**(1), 143.
55 D. Sloboda Rozner, P. L. Alsters and R. Neumann, *J. Am. Chem. Soc.*, 2003, **125**(18), 5280.

56 R. Neumann and A. M. Khenkin, *J. Mol. Catal. A: Chem.*, 1996, **114**(1–3), 169.
57 Y. Kikukawa, K. Yamaguchi and N. Mizuno, *Inorg. Chem.*, 2010, **49**(18), 8194.
58 M. Bösing, I. Loose, H. Pohlmann and B. Krebs, *Chem. – Eur. J.*, 1997, **3**(8), 1232.
59 B. Ravel and M. Newville, *J. Synchrotron Radiat.*, 2005, **12**(Pt 4), 537.
60 A. L. Ankudinov, B. Ravel, J. J. Rehr and S. D. Conradson, *Phys. Rev. B: Condens. Matter Mater. Phys.*, 1998, **58**(12), 7565.
61 A. D. Becke, *Phys. Rev. A*, 1988, **38**(6), 3098.
62 J. P. Perdew, *Phys. Rev. B: Condens. Matter Mater. Phys.*, 1986, **33**(12), 8822.
63 T. H. Dunning and P. J. Hay, in *Methods of electronic structure theory*, ed. H. F. Schaefer, Springer Science+Business Media, LLC, New York, 1977, p. 1.
64 F. Weigend and R. Ahlrichs, *Phys. Chem. Chem. Phys.*, 2005, **7**(18), 3297.
65 P. J. Hay and W. R. Wadt, *J. Chem. Phys.*, 1985, **82**(1), 299.
66 P. J. Hay and W. R. Wadt, *J. Chem. Phys.*, 1985, **82**(1), 270.
67 W. R. Wadt and P. J. Hay, *J. Chem. Phys.*, 1985, **82**(1), 284.
68 A. Klamt and G. Schüürmann, *J. Chem. Soc., Perkin Trans. 2*, 1993, **5**, 799.
69 K. Baldridge and A. Klamt, *J. Chem. Phys.*, 1997, **106**(16), 6622.
70 A. Klamt, V. Jonas, T. Bürger and J. C. W. Lohrenz, *J. Phys. Chem. A*, 1998, **102**(26), 5074.
71 M. D. Hanwell, D. E. Curtis, D. C. Lonie, T. Vandermeersch, E. Zurek and G. R. Hutchison, *J. Cheminf.*, 2012, **4**(1), 17.
72 http://www.webmo.net/index.html.
73 M. G. Tucker, D. A. Keen, M. T. Dove, A. L. Goodwin and Q. Hui, *J. Phys.: Condens. Matter*, 2007, **19**(33), 335218.
74 C. A. Triana, C. M. Araujo, R. Ahuja, G. A. Niklasson and T. Edvinsson, *Sci. Rep.*, 2017, **7**(1), 2044.
75 C. A. Triana, C. M. Araujo, R. Ahuja, G. A. Niklasson and T. Edvinsson, *Phys. Rev. B*, 2016, **94**(16), 165129.
76 E. Tanuhadi, A. Roller, G. Giester, I. Kampatsikas and A. Rompel, *Dalton Trans.*, 2018, **47**(44), 15651.
77 J. Cho, S. Jeon, S. A. Wilson, L. V. Liu, E. A. Kang, J. J. Braymer, M. H. Lim, B. Hedman, K. O. Hodgson, J. S. Valentine, E. I. Solomon and W. Nam, *Nature*, 2011, **478**(7370), 502.
78 R. Banerjee, Y. Proshlyakov, J. D. Lipscomb and D. A. Proshlyakov, *Nature*, 2015, **518**(7539), 431.
79 R. H. Ingle, N. K. Kala Raj and P. Manikandan, *J. Mol. Catal. A: Chem.*, 2007, **262**(1–2), 52.
80 N. J. Campbell, A. C. Dengel, C. J. Edwards and W. P. Griffith, *J. Chem. Soc., Dalton Trans.*, 1989, **6**, 1203.
81 C. Aubry, G. Chottard, N. Platzer, J. M. Bregeault, R. Thouvenot, F. Chauveau, C. Huet and H. Ledon, *Inorg. Chem.*, 1991, **30**(23), 4409.
82 R. Sheldon, I. Arends and A. Dijksman, *Catal. Today*, 2000, **57**(1–2), 157.
83 W. Adam, P. L. Alsters, R. Neumann, C. R. Saha-Möller, D. Sloboda-Rozner and R. Zhang, *Synlett*, 2002, **12**, 2011.
84 A. M. Morris, O. P. Anderson and R. G. Finke, *Inorg. Chem.*, 2009, **48**(10), 4411.
85 K. Nakajima, K. Eda and S. Himeno, *Inorg. Chem.*, 2010, **49**(11), 5212.
86 J. Niu, Z. Wang and J. Wang, *J. Coord. Chem.*, 2004, **57**(15), 1271.
87 C. Ci, H. Liu, L. Yan and Z. Su, *ChemistryOpen*, 2016, **5**(5), 470.